Chemical Engineering Journal 392 (2020) 123736

Contents lists available at ScienceDirect

Chemical Engineering Journal

journal homepage: www.elsevier.com/locate/cej

Dimensional-dependent antibacterial behavior on bioactive micro/nano polyetheretherketone (PEEK) arrays

Shi Mo[a,b,1], Babak Mehrjou[a,1], Kaiwei Tang[a], Huaiyu Wang[b], Kaifu Huo[c], Abdul Mateen Qasim[a], Guomin Wang[a,*], Paul K. Chu[a,*]

[a] Department of Physics, Department of Materials Science and Engineering, and Department of Biomedical Engineering, City University of Hong Kong, Tat Chee Avenue, Kowloon, Hong Kong, China
[b] Shenzhen Institutes of Advanced Technology, Chinese Academy of Sciences, Shenzhen, China
[c] Wuhan National Laboratory for Optoelectronics (WNLO), School of Optical and Electronic Information, Huazhong University of Science and Technology, Wuhan, China

HIGHLIGHTS

- Different micro- and nano-structured polyetheretherketone (PEEK) arrays are prepared.
- The antibacterial behavior depends on the topography.
- Stretching distortion is triggered to prevent self-adjustment of bacteria.
- The hybrid structures cause physical distortion of bacteria.
- The arrays improve the bioactivity of PEEK.

GRAPHICAL ABSTRACT

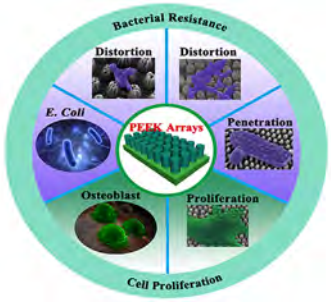

ARTICLE INFO

Keywords:
Micro/nano-arrays
Antibacterial surface
Bio-inspired materials
Polyetheretherketone

ABSTRACT

Polyetheretherketone (PEEK) is a biocompatible polymer but the poor bacteria resistance and bioactivity have hampered its wider application to orthopedics. Inspired by the natural antibacterial structure on insect wings, cone/pillar-like micro/nano-arrays are fabricated controllably on PEEK by colloidal lithography and plasma etching and the resulting bacterial resistance and biocompatibility are investigated. The surface-engineered PEEK possesses enhanced antibacterial properties and the underlying mechanism depends on the surface topography and dimensions of the surface structures. With regard to the microarrays, both the early mechanical stretching effect and subsequent dimensional effect contribute to the overall antibacterial effects. On the other hand, the nanoarrays that mimic cicada wings kill bacteria solely by the penetration effect. Enhanced proliferation of osteoblasts is also observed from the modified PEEK rendering it suitable for implant materials. The antibacterial principles concluded from this work provide insights into the design and fabrication of bio-inspired biomaterials with improved bacteria resistance and biocompatibility.

1. Introduction

In order to mitigate post-surgery bacterial infection, implants with both bacteria resistance and osteoconductivity are desirable for biomedical engineering [1,2]. Bactericidal agents and antibiotics can be introduced but there are potential side effects such as toxicity and

* Corresponding authors.
E-mail addresses: guomiwang2-c@my.cityu.edu.hk (G. Wang), paul.chu@cityu.edu.hk (P.K. Chu).
[1] Made equal contributions.

https://doi.org/10.1016/j.cej.2019.123736
Received 23 September 2019; Received in revised form 2 December 2019; Accepted 5 December 2019
Available online 07 December 2019
1385-8947/

development of bacterial resistance [3–5]. The antibacterial behavior has been observed from some natural surfaces such as insect wings consequently spurring research of new antibacterial methods without the use of extraneous chemicals [6,7]. Nanostructures kill bacteria by applying physical stress to the bacteria membrane causing rupture and death, but the effects of different types of micro-nano structures and associated mechanisms are not well understood [8,9]. Since bacteria can build their own networks according to the surroundings such as micropatterned poly(dimethylsiloxane), it is important to understand the topography-based bacteria-killing process and how the antibacterial efficiency varies with the dimensions, mechanical properties, and chemical composition of the surface structure [10].

Surface structures with different topographies such as arrays can be prepared by anodic techniques using the aluminum oxide (AAO) template as well as lithographic techniques, but the former cannot be extended to the micrometer range and the latter is usually time consuming and complex [11,12]. In this respect, colloidal lithography is a flexible technique to prepare arrays with nano and micro dimensions [13]. Combined with plasma etching, colloidal lithography has been utilized to prepare various surface structures by adjusting the mask size, plasma source, and etching process [14]. More importantly, it is a surface engineering technique that does not alter the favorable bulk attributes of the materials and therefore, it is very attractive to biomaterials. This technique may be used to construct array structures on materials such as titanium alloys and other biocompatible materials. In this study, polyetheretherketone (PEEK) is chosen as the model material.

PEEK has good biocompatibility and mechanical properties but limited bactericidal capability [15]. Although ion implantation and immersion in sulfuric acid have been employed to improve the bacterial resistance of PEEK, the chemical, mechanical, and structural properties are often altered as well [16–18]. In this work, micro/nano-arrays with different dimensions and densities are prepared on PEEK by self-assembly of polystyrene (PS) spheres and plasma etching (oxygen and argon). The shape, height, and interspatial distance of the arrays can be tailored by adjusting the plasma gas and etching parameters to achieve different biological effects and the associated mechanisms are investigated. Both the mechanical stretching effect during early contact with bacteria and subsequent dimensional effect are responsible for the bacteria-killing ability of microarrays, whereas the nanoarrays kill bacteria *via* a mechanism similar to that occurring on cicada wings. The biocompatibility is also improved due to the increased surface free energy after the plasma treatment. Our results reveal a controllable strategy to endow implants with topography-dependent mechanical antibacterial properties while the favorable bulk attributes of PEEK are preserved. The mechanistic study and conclusion also provide insights into the design and fabrication of biomaterials with multiple functions.

2. Experimental section

2.1. PEEK pretreatment

The medical-grade PEEK samples supplied by GEHR Plastics Hong Kong Ltd., Hong Kong were polished to a near mirror finish on one side, ultrasonically cleaned in anhydrous alcohol and ultra-pure water for 5 min sequentially, and dried under flowing nitrogen. The samples were treated with argon plasma for 2 min to increase the hydrophilicity before self-assembly of polystyrene (PS) spheres (BaseLine ChromTech Research Centre, Tianjin, China).

2.2. Micro/nano-arrays fabrication

The PS sphere monolayer was prepared by self-assembly. Briefly, a tilted glass slide was put on a petri dish filled with pure water. The 2 wt % PS suspension (water: ethanol = 1:1 (v/v)) was added dropwise (3 μL) to the glass slide and the PS spheres spread on the water surface to form monolayer automatically. By lifting the PEEK samples gently and drying them in air, the monolayer was transferred to the sample surface. The monolayers were visible to the naked eye thus verifying successful transfer of the PS spheres after lifting and drying. Monolayers with PS size of 320 nm and 1.5 μm were prepared to control the arrays on the PEEK substrate. In the next step, the samples with the PS monolayer were etched using a radio frequency (RF) Ar/O_2 plasma on the AJA sputtering system equipped with the 100/300 power source (AJA International, Inc. USA). Afterwards, the samples were cleaned in a water bath ultrasonically for 5 min to remove residual PS spheres and dried at 60 °C.

2.3. Materials characterization

The mechanical properties were determined on the Nano-indenter XP (MTS, USA) at room temperature at a rate of 10 nm s^{-1}. The water and diiodomethane contact angles were measured on the contact angle goniometer (Model 200, Rame-Hart, USA) and X-ray photoelectron spectroscopy (XPS, Thermo Fisher Scientific, USA) with Al K_α excitation (72 W) was performed to determine the chemical composition of the samples. The Fourier transform infrared (FTIR) spectra were recorded from 4,000 to 500 cm^{-1} (Frontier, PerkinElmer, USA) in the reflection mode with a resolution of 4 cm^{-1}. Prior to observation by scanning emission microscopy (SEM, JSM 820, JEOL, Japan), the samples were coated with a thin gold layer to circumvent charging. Atomic force microscopy (AFM) was conducted on the MultiMode V Microscope (Veeco, Bruker, USA) using the tapping mode at 0.5 Hz. The important AFM parameters were: spring constant = 40 N m^{-1}, tip radius = 6 nm, and resonance frequency = 300 kHz and at least three random areas were tested for each sample. The dimensional parameters of the arrays were determined from the AFM images and the roughness factor was calculated according to the following equation [19]:

$$\text{Roughness factor} = \frac{2 \times L \times \pi \times D_r}{\pi \times D_r^2}$$

where L represents the slant height and D_r is the diameter of the root.

2.4. Antibacterial assay

The antibacterial efficiency was determined by the spread plate method using *E. coli* (ATCC 25922). The bacteria were cultured while being agitated (220 rpm) in the Lysogeny Broth (LB) medium at 37 °C overnight and diluted to OD_{600} = 0.1. The suspension was diluted 100 times with physiological saline and 100 μL of the bacterial suspension were seeded on the sterilized samples on a 24-well plate for 3, 6, 12, and 24 h. Afterwards, 900 μL of the LB medium were added to the samples and mixed with the culture medium by pipetting. 10 μL of the bacterial suspension were spread on an agar plate and incubated at 37 °C for 15 h before counting the colony-forming unit (CFU). The bactericidal efficiency was calculated by the following equation:

$$\text{Bactericidal efficiency} = \frac{CFU_{control} - CFU_{test}}{CFU_{control}}$$

2.5. SEM observation and AFM analysis

The 10-times diluted bacterial suspension was spread on the samples and incubated on 24-well plates at 37 °C for 6 h. The samples were rinsed with the phosphate-buffered saline (PBS, pH = 7.4) three times and immersed in glutaraldehyde to immobilize the attached *E. coli*. The samples were then dehydrated with 10%, 30%, 50%, 70%, 90%, and anhydrous ethanol for 20 min each and dried at 37 °C. The morphology of the bacteria was inspected after gold coating. Before AFM analysis of the attached bacteria, the samples were fixed with glutaraldehyde for 4 h and dehydrated with a series of alcohol (10%, 30%, 50%, 70%, 90%, and anhydrate) to eliminate interferences from water.

2.6. Bacterial intracellular species measurement and fluorescent staining

The intracellular species released from the bacteria reflects the integrity of the bacterial cell membrane. To obtain reliable values, the suspension of *E. coli* (OD_{600} = 0.2) was centrifuged at 8,000 rpm for 10 min to remove the supernatant and re-suspended with the fresh PBS buffer (pH = 7.4). The procedure was repeated to remove the LB medium. 100 μL of the bacteria-PBS suspension were introduced to the samples and incubated for 6 h. After incubation, the culture medium was diluted 10 times with PBS and the samples were treated ultrasonically for 5 min to dissociate the intracellular species from the surface. The bacteria extracted were centrifuged at 8,000 rpm for 10 min and 100 μL of the supernatant were transferred to a 96-well plate to measure the absorbance (260 nm, Multimode microplate reader, Bio Tek, USA).

To stain the bacteria, the bacterial suspension (OD_{600} = 0.1) was diluted 100 times and cultured on the PEEK sample for 6 h. Afterwards, the bacterial medium was removed. The adherent bacteria were stained with the bacterial viability kit (L7012, Molecular Probes, Eugene, USA) and washed 5 times with PBS. The fluorescent images were captured by an inverted fluorescent microscope (Axiovert 40, Zeiss, Germany).

2.7. Cell culture and viability

The osteoblastic cells (MC3T3-E1) provided by the cell bank (Chinese Academy of Sciences) were cultured on petri dishes with the Dulbecco's modified eagle medium (DMEM, Life Technologies, Canada) containing 10% fetal bovine serum (FBS) and kept in an incubator at 37 °C under 5% CO_2. The MTT (3-(4,5-dimethylthiazol-2-yl)-2,5-diphenyl tetrazolium bromide, Sigma-Aldrich, USA) assay was applied to assess the viability of the osteoblasts quantitatively. Before the experiment, the cells were harvested with trypsin (Life Technologies, Canada), centrifuged (1,000 rpm, 5 min) and adjusted to approximately 2×10^4 cells mL^{-1} with the fresh medium. Half a mL of the cell containing medium was seeded on the samples on a 24-well plate and cultured for 1, 4, and 7 days. At each time point, the samples were moved to a new 24-well plate and immersed in 500 μL of the DMEM (FBS free) - MTT solution for 4 h. Subsequently, the MTT solution was replaced by DMSO (dimethyl sulfoxide) to dissolve the formazan crystals produced by the osteoblasts. The absorbance of formazan (570 nm) was recorded on a microplate reader (BioTek, USA) using 100 μL of the DMSO solution on a 96-well plate with pure DMSO being the control.

2.8. Cell morphology

The MC3T3-E1 cells were seeded on the samples and incubated for 1 day as mentioned above. After culturing, the cells were rinsed gently with PBS twice, fixed with paraformaldehyde (4% v/v) overnight, dehydrated by the aforementioned procedures, and dried in an incubator. All the samples were coated with gold to prevent charging before microscopic examination.

2.9. Statistical analysis

Each measurement was repeated at least 3 times. The data were analyzed by the single factor ANOVA and shown as mean ± standard deviation (SD).

3. Results and discussion

3.1. Materials preparation

The preparation process is illustrated in Fig. 1a. By using a self-assembled monolayer of micro/nano-spheres and performing plasma etching, large-area arrays of micro or nano surface structures are fabricated. The ordered templates that control the size and interspatial distance of the arrays are prepared by forming a closely packed monolayer of PS spheres with two different sizes of 320 nm and 1.5 μm. The 1.5 μm PS spheres are chosen in our experiments because the arrays have a similar size and interspace as *E. coli* and are quite straightforward to produce. The micro/nano-arrays are then formed by plasma etching under different conditions (Fig. S1).

After preparation of the PS sphere monolayers (Fig. 1b), plasma etching is conducted with different gases at the same pressure, plasma power, and etching time. The argon plasma is an anisotropic etching process. By etching the monolayer in the vertical direction, the monolayer is unchanged in the horizontal direction (Fig. 1c). On the other hand, during oxygen plasma etching, the PS spheres are etched isotropically and the size of the PS spheres decreases (Fig. 1d) [20,21]. After the Ar plasma treatment, the PS spheres become inert and can hardly be etched in the horizontal direction by the oxygen plasma.

According to the above observations, arrays with the pre-designed dimensions are prepared by adjusting the etching process and gas. To produce the pillar-like arrays, the PEEK-PS sample is etched with an Ar plasma for 30 min and then oxygen plasma for 80 min (Fig. 1e). To prepare the cone-like arrays, the sample is treated with the oxygen plasma solely for 80 min (Fig. 1f). The nanocones (NC), nanopillars (NP), microcones (MC), and micropillars (MP), and corresponding fabrication parameters are presented in Table S1. For comparison, PEEK samples without monolayers are prepared with argon and oxygen plasmas and denoted as PEEK-O and PEEK-Ar, respectively. However, only disordered nanostructures can be found (Fig. S1a and b).

3.2. Characterization

The dimensional parameters of the arrays determined by AFM (Fig. S1) are shown in Fig. 2a.

The roughness factor of the array structure is chosen as the representative parameter of the structure [19]. Although the roughness factors of the four arrays are similar (Fig. 2b), the dimensions and shape are quite different. Generally, the height (H) and top diameter (D_t) of the pillar arrays are larger than those of the cone arrays. However, the inter-distance (S) exhibits the reverse trend. It may be ascribed to the passivation effect of the Ar plasma and high reactivity of the O_2 plasma with respect to the PS monolayer (Fig. 2c and 2d). After the plasma treatment, the PEEK surface becomes hydrophilic as indicated by a slightly larger oil contact angle (Fig. S2a) boding well for cell attachment [22–24]. It is noted that although these dimensional parameters have been reported to be important to cell attachment and bacteria killing [25], the antibacterial mechanisms of these microscale and nanoscale structures are not well understood.

The chemical composition of the pristine PEEK, PEEK-O, and MP is determined by X-ray photoelectron spectroscopy (XPS). As shown in Fig. S2b, the C ls peak becomes weaker after the oxygen plasma treatment indicating a smaller carbon concentration but on the other hand, the O 1s peak becomes stronger. The oxygen concentration exceeds 20% and nearly doubles that of the pristine PEEK (Table S2). Compared to the pristine PEEK, both PEEK-O and MP exhibit weaker C1 peaks (C−C, C−H) but stronger C2 (C−O) and C3 (C═O) peaks (Fig. S2c–e) and the observation is in line with previous one suggesting enrichment of polar groups after etching. However, the C1 peak decreases by nearly 30% due to long-term exposure to the plasma, compared to 10% to 18% reduction observed after short-term oxygen plasma etching or air-plasma activation [26,27]. As aforementioned, the polar groups decrease the water contact angles and increase the surface energy (Table S2), which in turn affects the bacteria attachment and cytocompatibility [28–30].

The chemical change is further analyzed by Fourier transform infrared spectroscopy (FTIR). The peaks originating from the rotation of the aromatic ring (1412 cm^{-1}), asymmetric stretching of the aromatic ring (1156 cm^{-1}), and asymmetric stretching of C−O−C (1188 cm^{-1}) are weaker after plasma etching (Fig. 2e) due to movement of the ether

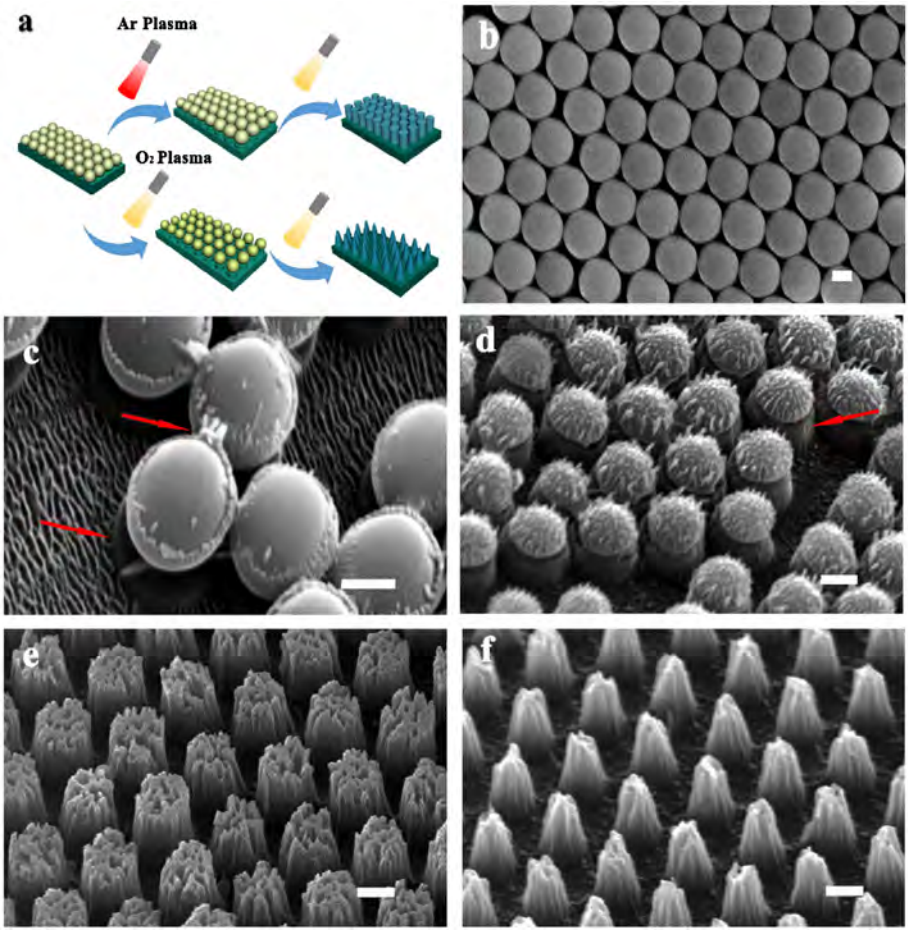

Fig. 1. (a) Schematic illustration of the preparation of the arrays; (b) SEM image of the self-assembled polystyrene (PS) monolayer on the PEEK surface; (c) SEM image of the PS spheres and PEEK substrate after argon plasma etching for 30 min; (d) SEM image of the PS spheres after oxygen plasma etching for 30 min; (e) SEM image of the pillar-like microarray (MP) prepared by argon and oxygen plasma etching in succession; (f) SEM image of the cone-like microarray (MC) prepared by oxygen plasma only. The scale bar is 1 μm.

linkage [31]. However, these peaks do not shift and there are no new peaks and shoulders, demonstrating that after the plasma treatment, the ratio of C to O is changed but no new chemical structure is created.

With a lower elastic modulus than metals, PEEK is more suitable for bone implants because of the smaller mechanical mismatch *in vivo* [32]. Here, the hardness and elastic modulus are measured to assure that the bulk properties of PEEK are preserved after the plasma treatment (Fig. 2f). The elastic modulus changes only slightly in the range of 3–5.5 GPa and although the hardness of MP and MC decreases, the clinical impact is minimal [33]. All in all, the mechanical properties are maintained after the plasma treatment, but the modified surface properties are expected to play important roles in the bacterial resistance and cell growth.

3.3. Antibacterial properties and mechanisms

E. coli, a common Gram-negative bacterium with a rod shape, size of 0.5–1 μm, and cell membrane thickness of about 10 nm, serves as the model bacteria [34]. The nanostructure created by the oxygen plasma without a mask has limited bactericidal effects but arrays with different morphology kill bacteria with a certain trend (Fig. 3a). In general, microarrays show better antibacterial rates than nanoarrays with MP and MC achieving 2-log and 1-log reduction, respectively. With regard to the nanoarrays, NC performs better than NP (80–90% versus 75–80%).

Rupture of the cell membrane sometimes cannot kill bacteria if the temporary stress on the membrane is removed because the wound can heal automatically [35]. Hence, the released intracellular components such as DNA and RNA are analyzed to assess the integrity of the cell membrane [36]. The amount of the intracellular species released from the bacteria on MP is the largest revealing serious membrane rupture consistent with the antibacterial trend observed from the CFU counting results (Fig. 3b and 3c). The results show that the ruptured bacteria cannot be revived. The fluorescent images (Fig. 3d) taken from the bacteria on the PEEK samples also confirm reduction of viable *E. coli*. However, owing to strong auto-fluorescence from PEEK, red fluorescence of dead bacteria can hardly be observed.

The morphological change of treated bacteria is further assessed to elucidate the antibacterial mechanism. Compared to the untreated sample (Fig. 4a), the bacteria on PEEK-O (Fig. 4b) become longer and exhibit a division behavior. The bacteria on the nanoarrays react similarly to those on cicada wings as shown by a previous study [9]. With regard to NP, the bacteria do not have to change the shape to fit the pillar-like structure and some of them are still healthy (Fig. 4c). It is evident that the sharper tip and smaller cone density of NC compared to NP give rise to better efficacy concerning membrane penetration [37,38]. The successive interactions between NC and bacteria facilitate rupture of the membrane leading to death. The bacteria attached to the surface of NC (Fig. 4d) show three states. Some are completely penetrated and killed by the arrays while some shriveled cells are in a dying state. However, some bacteria remain alive by bending the arrays indicating that some *E. coli* cells can survive on the tips of the nanoarrays by adjusting their shape. This phenomenon may limit the antibacterial performance and arrays with optimized aspect ratios may improve the effect. In comparison, the bacteria on the microarrays are more severely distorted and their original shape can hardly be observed (Fig. 4e and 4f). It may be the result of the combination of the mechanical, dimensional, and morphological effects of MC and MP [39].

Compared to the nanoarrays, the microarrays have hybrid structures with micrometer and sub-micrometer dimensions. Besides, the

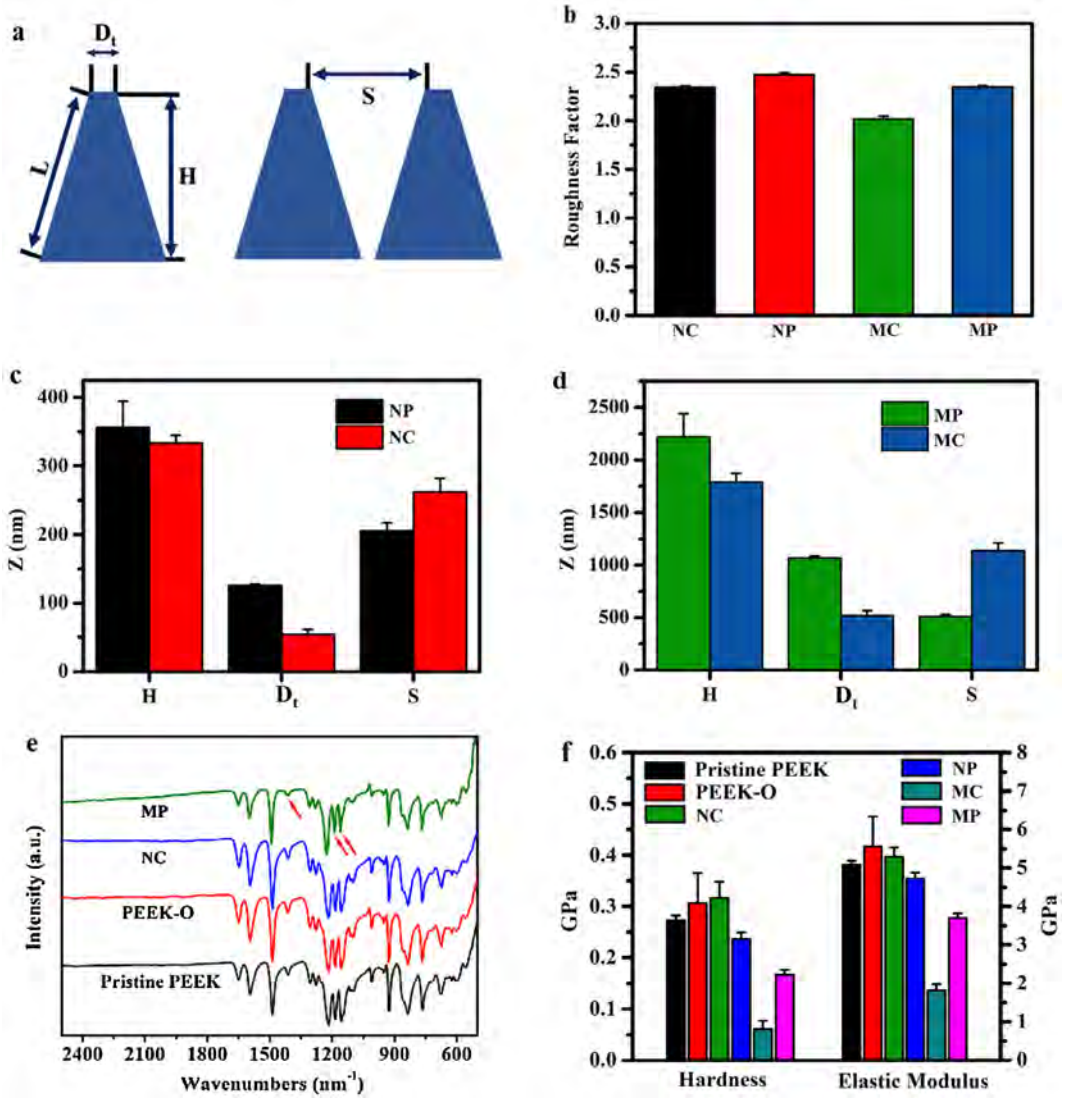

Fig. 2. (a) Schematic illustration of the arrays on PEEK with the top diameter of the array being D_t, height of the array being H, slant height being L, and S denoting the distance between the two arrays regardless of the shape of the array; (b) Roughness factors of the PEEK samples; Dimensions of (c) Nanoarrays (NP and NC) and (d) Microarrays (MP and MC); (e) FTIR spectra; (f) Hardness and elastic modulus values.

lateral structure of these microarrays is sheet-like which can easily impose a tangential force on the attached bacteria. Therefore, bacteria on the microarrays face a harsher environment and in fact, the microarrays and nanoarrays show different mechanisms with the narrow-interspaced MP surpassing MC. D_t and S of MP are about 1 μm and 0.5 μm, respectively, and most of the *E. coli* cells stay on top of the bumpy surface. Therefore, they are easily distorted and killed due to the strong adhesion between the bacteria and PEEK surface. MP with a long array, large density, and hybrid structure has the best antibacterial ability [40]. In the case of MC, S is larger (around 1.2 μm) and the bacteria stay at a distance instead of residing on the surface. The antibacterial performance relies more on the tangential force on the lateral surface while the rupturing effect rendered by the tips is minimal (Fig. 4e). Hence, it can be inferred that the sheet-like structure on MC can rupture the membrane of *E. coli* physically similar to that observed from vertically aligned graphene oxide nanosheets [41–43]. As discussed above, when filling the interspace, the bacteria have to change shape to adapt to the microarray. Therefore, they are distorted severely by the hybrid structure of MC and the mechanism is different from that of the nanoarrays on which bacteria can maintain the original shape.

The interactive stress between bacteria and surface is crucial to the antibacterial process on the micro/nano-arrays and quantitative comparison of the adhesion stress can offer some clues about the antibacterial mechanism. The degree of deflection of the AFM tip can be exploited to determine the adhesion force (Fig. S3) [44]. In general, the plasma-treated PEEK samples facilitate bacteria adhesion albeit by a different degree due to the change in the surface energy and surface structure (Fig. 4g). With regard to the nanoarrays, the smaller adhesion force causes limited stretching of the bacteria on the surface and as a result, only the penetration effect caused by the sharp tips is significant [45]. In the early stage of contact, strong adhesion exacerbates stretching of the bacteria and the dimensional effect becomes dominant in rupturing the bacteria as confirmed by SEM (Fig. 4e and f). Although bacteria can adjust to environmental changes to some extent, the imbalance between self-adaption and distorting caused by the microarrays finally leads to death of *E. coli*.

3.4. Biocompatibility

MC3T3-E1 osteoblasts are employed to evaluate the cell viability and proliferation [46] and quantitative assessment is carried out by the MTT assay based on that the absorbance of formazan is proportional to

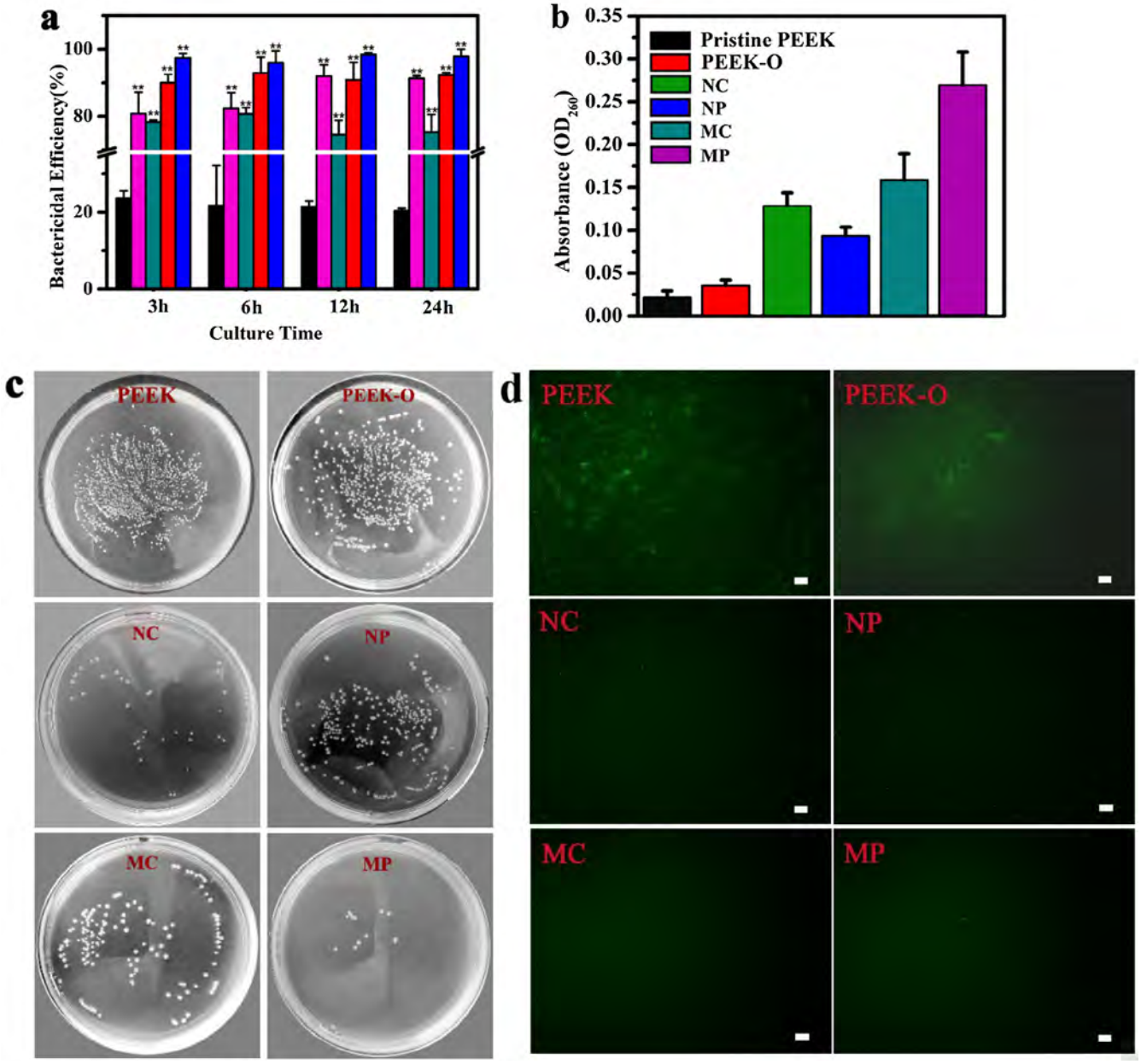

Fig. 3. (a) Antibacterial efficiency of PEEK-O (black), NC (magenta), NP (dark cyan), MC (red), and MP (blue) for different culturing periods (** denotes significant difference compared to PEEK-O ($p < 0.05$)); (b) Absorbance of intercellular species released from *E. coli* measured at 260 nm; (c) Pictures of the petri dishes after culturing for 6 h; (d) Fluorescent images of the bacteria on the PEEK samples. The scale bar is 20 μm. (For interpretation of the references to colour in this figure legend, the reader is referred to the web version of this article.)

the number of living cells [47]. The results show clearly that the arrays on PEEK improve cell growth compared to the pristine PEEK (Fig. 5a).

Growth of MC3T3-E1 cells on all the arrays displays a positive trend from the 1st to 7th day. Although the high stress derived from MP affects cell attachment, the cell viability increases and the highest proliferation rate is observed on the 7th day. In contrary to *E. coli*, the larger MC3T3-E1 cells can grow well on the arrays by adjusting themselves to the surface topography. As shown in Fig. 5b, a few cells attach to the surface of the pristine PEEK after the 1st day. They just begin to organize the vinculin around themselves. In comparison, obvious cell spreading is observed from Fig. 5c, 5d, and 5e, demonstrating that oxygen plasma treatment creates a more friendly environment to foster cell growth [48]. The MC3T3-E1 cells can attach, spread, and proliferate on the pillars or cones with diameters between 100 nm and 1 μm. The MTT assay and SEM images show that osteoblasts prefer a rough surface as consistent with other studies [28,49,50] and the MC3T3-E1 cells are not inhibited on these arrays on account of their large size and shape [51,52]. All in all, the microarrays and nanoarrays constructed on PEEK by this technique are both bactericidal and biocompatible and have large clinical potential.

Recent research on improving the antibacterial ability of PEEK has mainly focused on the incorporation of antibacterial substances such as silver [53] and fluoro-hydroxyapatite [54]. Although these modification schemes like ion implantation and deposition can indeed improve the antibacterial properties, there are drawbacks including deleterious side-effects arising from the potential toxicity due to excessive release of extraneous antibacterial agents and additional chemical reactions that require a longer time to produce the effects [17,55]. In comparison, the modified surface described here kills bacteria based on physical interactions only and no side effects are produced.

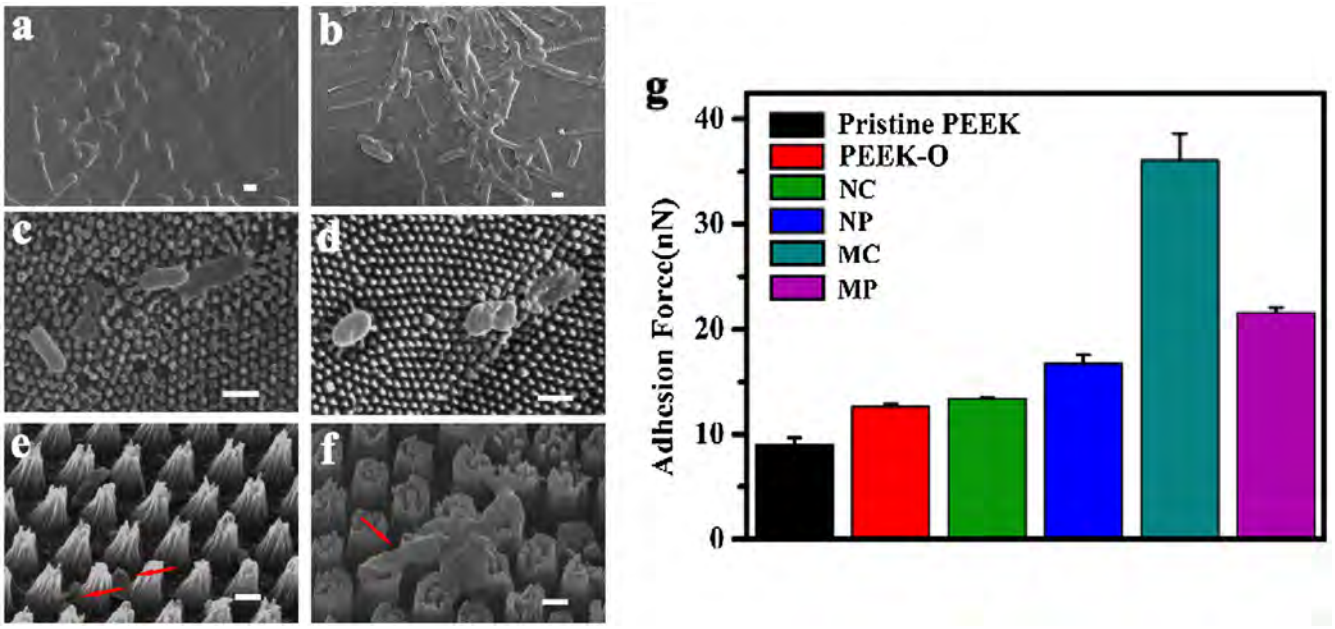

Fig. 4. SEM images showing the morphology of *E. coli* on the different PEEK samples: (a) Pristine PEEK, (b) PEEK-O, (c) NC, (d) NP, (e) MC, and (f) MP after culturing for 6 h (Scale bar = 1 μm); (g) Adhesion force between the bacteria and PEEK measured by AFM.

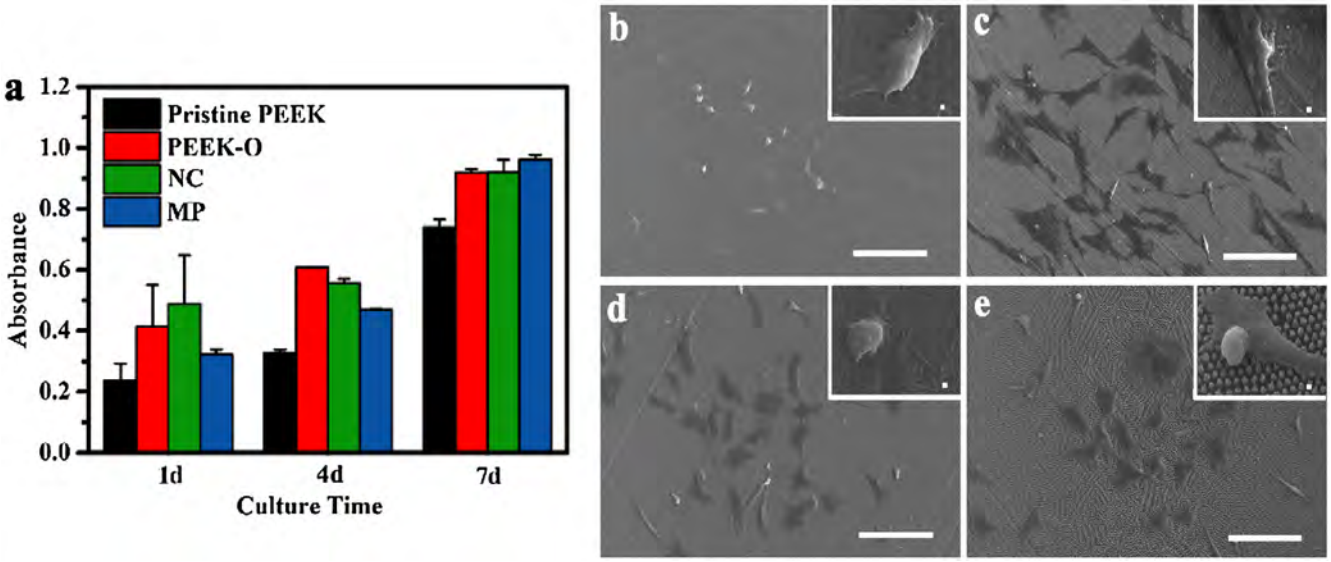

Fig. 5. (a) MTT assay results of the pristine PEEK, PEEK-O, NC, MP for different periods; Images of the MC3T3-E1 cells on (b) Pristine PEEK, (c) PEEK-O, (d) NC, and (e) MP after incubation for 1 day. The scale bar is 100 μm (Insets are the corresponding enlarged images, and the scale bar is 1 μm).

4. Conclusion

A series of bactericidal structures composed of pillar-like and cone-like micro/nano-arrays are fabricated by adjusting the size of the mask and parameters in plasma etching. Both the PEEK nanoarrays and microarrays kill *E. coli* but the mechanisms are different. The nanoarrays impose stress and penetrate the cell membrane similar to the bacterial killing mechanism on cicada wings. NC with sharper tips exhibits better bacterial resistance than NP. With regard to the microarrays, owing to the stronger adhesion, the *E. coli* cells are deformed more effectively and the hybrid structure of the microarrays can better offset the self-adjusting behavior of the bacteria as observed from NC. In conjunction with the improved cell viability, the surface-modified PEEK materials have large clinical potential. The mechanisms revealed in this study provide a better understanding of the interactions between the bacteria/cells and surface topography enabling the design and fabrication of new biomaterials with multiple functions.

Declaration of Competing Interest

The authors declare that they have no known competing financial interests or personal relationships that could have appeared to influence the work reported in this paper.

Acknowledgments

Shi Mo and Babak Mehrjou made equal contributions to the work. The authors acknowledge the financial support provided by the Hong Kong Research Grants Council (RGC) General Research Funds (GRF) No. CityU 11205617 and City University of Hong Kong Strategic Research Grant (SRG) No. 7005264.

Appendix A. Supplementary data

Supplementary data to this article can be found online at https://doi.org/10.1016/j.cej.2019.123736.

References

[1] C.R. Arciola, D. Campoccia, L. Montanaro, Implant infections: adhesion, biofilm formation and immune evasion, Nat. Rev. Microbiol. 16 (2018) 397–409, https://doi.org/10.1038/s41579-018-0019-y.

[2] J. Liao, W. Chen, M. Yang, J. Zhou, Z. Wang, Y. Zhou, C. Ning, H. Yuan, Conducting photopolymers on orthopeadic implants having a switch of priority between promoting osteogenic and antibacterial activity, Mater. Horiz. 5 (2018) 545–552, https://doi.org/10.1039/C8MH00285A.

[3] G. Li, S. Yu, W. Xue, D. Ma, W. Zhang, Chitosan-graft-PAMAM loading nitric oxide for efficient antibacterial application, Chem. Eng. J. 347 (2018) 923–931, https://doi.org/10.1016/j.cej.2018.04.159.

[4] Y. Liang, M. Wang, Z. Zhang, G. Ren, Y. Liu, S. Wu, J. Shen, Facile synthesis of ZnO QDs@GO-CS hydrogel for synergetic antibacterial applications and enhanced wound healing, Chem. Eng. J. 378 (2019) 122043, , https://doi.org/10.1016/j.cej.2019.122043.

[5] G. Wang, H. Feng, L. Hu, W. Jin, Q. Hao, A. Gao, X. Peng, W. Li, K.-Y. Wong, H. Wang, Z. Li, P.K. Chu, An antibacterial platform based on capacitive carbon-doped TiO_2 nanotubes after direct or alternating current charging, Nat. Commun. 9 (2018) 2055, https://doi.org/10.1038/s41467-018-04317-2.

[6] K. Modaresifar, S. Azizian, M. Ganjian, L.E. Fratila-Apachitei, A.A. Zadpoor, Bactericidal effects of nanopatterns: a systematic review, Acta Biomateria. 83 (2019) 29–36, https://doi.org/10.1016/j.actbio.2018.09.059.

[7] E.P. Ivanova, J. Hasan, H.K. Webb, G. Gervinskas, S. Juodkazis, V.K. Truong, A.H.F. Wu, R.N. Lamb, V.A. Baulin, G.S. Watson, J.A. Watson, D.E. Mainwaring, R.J. Crawford, Bactericidal activity of black silicon, Nat. Commun. 4 (2013) 2838, https://doi.org/10.1038/ncomms3838.

[8] C.D. Bandara, S. Singh, I.O. Afara, A. Wolff, T. Tesfamichael, K. Ostrikov, A. Oloyede, Bactericidal effects of natural nanotopography of dragonfly wing on *Escherichia coli*, ACS Appl. Mater. Interfaces 9 (2017) 6746–6760, https://doi.org/10.1021/acsami.6b13666.

[9] E.P. Ivanova, J. Hasan, H.K. Webb, V.K. Truong, G.S. Watson, J.A. Watson, V.A. Baulin, S. Pogodin, J.Y. Wang, M.J. Tobin, C. Löbbe, R.J. Crawford, Natural bactericidal surfaces: mechanical rupture of *Pseudomonas aeruginosa* cells by cicada wings, Small 8 (2012) 2489–2494, https://doi.org/10.1002/smll.201200528.

[10] Z. Jahed, H. Shahsavan, M.S. Verma, J.L. Rogowski, B.B. Seo, B. Zhao, T.Y. Tsui, F.X. Gu, M.R.K. Mofrad, Bacterial networks on hydrophobic micropillars, ACS Nano 11 (2017) 675–683, https://doi.org/10.1021/acsnano.6b06985.

[11] A.M. Md Jani, D. Losic, N.H. Voelcker, Nanoporous anodic aluminium oxide: advances in surface engineering and emerging applications, Prog. Mater. Sci. 58 (2013) 636–704, https://doi.org/10.1016/j.pmatsci.2013.01.002.

[12] X. Ye, L. Qi, Two-dimensionally patterned nanostructures based on monolayer colloidal crystals: controllable fabrication, assembly, and applications, Nano Today 6 (2011) 608–631, https://doi.org/10.1016/j.nantod.2011.10.002.

[13] Y. Ke, S. Ye, P. Hu, H. Jiang, S. Wang, B. Yang, J. Zhang, Y. Long, Unpacking the toolbox of two-dimensional nanostructures derived from nanosphere templates, Mater. Horiz. 6 (2019) 1380–1408, https://doi.org/10.1039/C9MH00065H.

[14] B. He, Y. Yang, M.F. Yuen, X.F. Chen, C.S. Lee, W.J. Zhang, Vertical nanostructure arrays by plasma etching for applications in biology, energy, and electronics, Nano Today 8 (2013) 265–289, https://doi.org/10.1016/j.nantod.2013.04.008.

[15] X. Liu, K. Gan, H. Liu, X. Song, T. Chen, C. Liu, Antibacterial properties of nano-silver coated PEEK prepared through magnetron sputtering, Dent. Mater. 33 (2017) e348–e360, https://doi.org/10.1016/j.dental.2017.06.014.

[16] L. Ouyang, Y. Zhao, G. Jin, T. Lu, J. Li, Y. Qiao, C. Ning, X. Zhang, P.K. Chu, X. Liu, Influence of sulfur content on bone formation and antibacterial ability of sulfonated PEEK, Biomaterials 83 (2016) 115–126, https://doi.org/10.1016/j.biomaterials.2016.01.017.

[17] K. Gan, H. Liu, L. Jiang, X. Liu, X. Song, D. Niu, T. Chen, C. Liu, Bioactivity and antibacterial effect of nitrogen plasma immersion ion implantation on polyetheretherketone, Dent. Mater. 32 (2016) e263–e274, https://doi.org/10.1016/j.dental.2016.08.215.

[18] A. Reyna-Valencia, S. Kaliaguine, M. Bousmina, Structural and mechanical characterization of poly(ether ether ketone) (PEEK) and sulfonated PEEK films: effects of thermal history, sulfonation, and preparation conditions, J. Appl. Polym. Sci. 99 (2006) 756–774, https://doi.org/10.1002/app.22551.

[19] G. Li, J. Li, C. Zhang, Y. Hu, X. Li, J. Chu, W. Huang, D. Wu, Large-area one-step assembly of three-dimensional porous metal micro/nanocages by ethanol-assisted femtosecond laser irradiation for enhanced antireflection and hydrophobicity, ACS Appl. Mater. Interfaces 7 (2015) 383–390, https://doi.org/10.1021/am506291f.

[20] E.M. Akinoglu, A.J. Morfa, M. Giersig, Understanding anisotropic plasma etching of two-dimensional polystyrene opals for advanced materials fabrication, Langmuir 30 (2014) 12354–12361, https://doi.org/10.1021/la500003u.

[21] A. Plettl, F. Enderle, M. Saitner, A. Manzke, C. Pfahler, S. Wiedemann, P. Ziemann, Non-close-packed crystals from self-assembled polystyrene spheres by isotropic plasma etching: adding flexibility to colloid lithography, Adv. Funct. Mater. 19 (2009) 3279–3284, https://doi.org/10.1002/adfm.200900907.

[22] M. Jurak, A.E. Wiacek, K. Terpiłowski, Properties of PEEK-supported films of biological substances prepared by the Langmuir-Blodgett technique, Colloids Surf. A: Physicochem. Eng. Aspects 510 (2016) 263–274, https://doi.org/10.1016/j.colsurfa.2016.09.048.

[23] K. Masamoto, S. Fujibayashi, T. Yabutsuka, T. Hiruta, B. Otsuki, Y. Okuzu, K. Goto, T. Shimizu, Y. Shimizu, C. Ishizaki, K. Fukushima, T. Kawai, M. Hayashi, K. Morizane, T. Kawata, M. Imamura, S. Matsuda, In vivo and in vitro bioactivity of a "precursor of apatite" treatment on polyetheretherketone, Acta Biomateria. 91 (2019) 48–59, https://doi.org/10.1016/j.actbio.2019.04.041.

[24] A.E. Wiącek, A. Gozdecka, M. Jurak, K. Przykaza, K. Terpiłowski, Wettability of plasma modified glass with bioglass layer in polysaccharide solution, Colloids Surf. A: Physicochem. Eng. Aspects 551 (2018) 185–194, https://doi.org/10.1016/j.colsurfa.2018.04.061.

[25] Y. Cheng, G. Feng, C.I. Moraru, Micro- and nanotopography sensitive bacterial attachment mechanisms: a review, Front. Microbiol. 10 (2019) 191, https://doi.org/10.3389/fmicb.2019.00191.

[26] A.E. Wiącek, K. Terpiłowski, M. Jurak, M. Worzakowska, Low-temperature air plasma modification of chitosan-coated PEEK biomaterials, Polym. Test. 50 (2016) 325–334, https://doi.org/10.1016/j.polymertesting.2016.01.020.

[27] S. Zhang, F. Awaja, N. James, D.R. McKenzie, A.J. Ruys, Autohesion of plasma treated semi-crystalline PEEK: comparative study of argon, nitrogen and oxygen, Colloids Surf. A: Physicochem. Eng. Aspects. 374 (2011) 88–95, https://doi.org/10.1016/j.colsurfa.2010.11.013.

[28] K. Anselme, Osteoblast adhesion on biomaterials, Biomaterials 21 (2000) 667–681, https://doi.org/10.1016/S0142-9612(99)00242-2.

[29] M. Werner, S.B.G. Blanquer, S.P. Haimi, G. Korus, J.W.C. Dunlop, G.N. Duda, D.W. Grijpma, A. Petersen, Surface curvature differentially regulates stem cell migration and differentiation via altered attachment morphology and nuclear deformation, Adv. Sci. 4 (2017) 1600347, https://doi.org/10.1002/advs.201600347.

[30] F. Variola, F. Vetrone, L. Richert, P. Jedrzejowski, J.-H. Yi, S. Zalzal, S. Clair, A. Sarkissian, D.F. Perepichka, J.D. Wuest, F. Rosei, A. Nanci, Improving biocompatibility of implantable metals by nanoscale modification of surfaces: an overview of strategies, fabrication methods, and challenges, Small 5 (2009) 996–1006, https://doi.org/10.1002/smll.200801186.

[31] D. Puhan, J.S.S. Wong, Properties of polyetheretherketone (PEEK) transferred materials in a PEEK-steel contact, Tribol. Int. 135 (2019) 189–199, https://doi.org/10.1016/j.triboint.2019.02.028.

[32] N.T. Evans, F.B. Torstrick, C.S. Lee, K.M. Dupont, D.L. Safranski, W.A. Chang, A.E. Macedo, A.S.P. Lin, J.M. Boothby, D.C. Whittingslow, R.A. Carson, R.E. Guldberg, K. Gall, High-strength, surface-porous polyether-ether-ketone for load-bearing orthopedic implants, Acta Biomateria. 13 (2015) 159–167, https://doi.org/10.1016/j.actbio.2014.11.030.

[33] S. Wu, X. Liu, K.W.K. Yeung, C. Liu, X. Yang, Biomimetic porous scaffolds for bone tissue engineering, Mater. Sci. Eng. R Rep. 80 (2014) 1–36, https://doi.org/10.1016/j.mser.2014.04.001.

[34] S. Pogodin, J. Hasan, V.A. Baulin, H.K. Webb, V.K. Truong, T.H. Phong Nguyen, V. Boshkovikj, C.J. Fluke, G.S. Watson, J.A. Watson, R.J. Crawford, E.P. Ivanova, Biophysical model of bacterial cell interactions with nanopatterned cicada wing surfaces, Biophys. J. 104 (2013) 835–840, https://doi.org/10.1016/j.bpj.2012.12.046.

[35] Z. Suo, R. Avci, M. Deliorman, X. Yang, D.W. Pascual, Bacteria survive multiple puncturings of their cell walls, Langmuir 25 (2009) 4588–4594, https://doi.org/10.1021/la8033319.

[36] X. Jia, I. Ahmad, R. Yang, C. Wang, Versatile graphene-based photothermal nanocomposites for effectively capturing and killing bacteria, and for destroying bacterial biofilms, J. Mater. Chem. B 5 (2017) 2459–2467, https://doi.org/10.1039/C6TB03084J.

[37] S.M. Kelleher, O. Habimana, J. Lawler, B. O' Reilly, S. Daniels, E. Casey, A. Cowley, Cicada wing surface topography: an investigation into the bactericidal properties of nanostructural features, ACS Appl. Mater. Interfaces 8 (2016) 14966–14974, https://doi.org/10.1021/acsami.5b08309.

[38] G. Hazell, P.W. May, P. Taylor, A.H. Nobbs, C.C. Welch, B. Su, Studies of black silicon and black diamond as materials for antibacterial surfaces, Biomater. Sci. 6 (2018) 1424–1432, https://doi.org/10.1039/C8BM00107C.

[39] F. Song, H. Koo, D. Ren, Effects of material properties on bacterial adhesion and biofilm formation, J. Dent. Res. 94 (2015) 1027–1034, https://doi.org/10.1177/0022034515587690.

[40] M. Michalska, F. Gambacorta, R. Divan, I.S. Aranson, A. Sokolov, P. Noirot, P.D. Laible, Tuning antimicrobial properties of biomimetic nanopatterned surfaces, Nanoscale 10 (2018) 6639–6650, https://doi.org/10.1039/C8NR00439K.

[41] E. Morales-Narváez, A. Merkoçi, Graphene oxide as an optical biosensing platform: a progress report, Adv. Mater. 1805043 (2018), https://doi.org/10.1002/adma.201805043.

[42] X. Lu, X. Feng, J.R. Werber, C. Chu, I. Zucker, J.-H. Kim, C.O. Osuji, M. Elimelech, Enhanced antibacterial activity through the controlled alignment of graphene oxide nanosheets, Proc. Natl. Acad. Sci. 114 (2017) E9793–E9801, https://doi.org/10.1073/pnas.1710996114.

[43] H.M. Hegab, A. ElMekawy, L. Zou, D. Mulcahy, C.P. Saint, M. Ginic-Markovic, The controversial antibacterial activity of graphene-based materials, Carbon 105 (2016) 362–376, https://doi.org/10.1016/j.carbon.2016.04.046.

[44] H.H.P. Fang, K.-Y. Chan, L.-C. Xu, Quantification of bacterial adhesion forces using atomic force microscopy (AFM), J. Microbiol. Meth. 40 (2000) 89–97, https://doi.org/10.1016/S0167-7012(99)00137-2.

[45] Z. Jahed, S. Molladavoodi, B.B. Seo, M. Gorbet, T.Y. Tsui, M.R.K. Mofrad, Cell responses to metallic nanostructure arrays with complex geometries, Biomaterials 35 (2014) 9363–9371, https://doi.org/10.1016/j.biomaterials.2014.07.022.

[46] L. LeGuehennec, M.-A. Lopez-Heredia, B. Enkel, P. Weiss, Y. Amouriq, P. Layrolle, Osteoblastic cell behaviour on different titanium implant surfaces, Acta Biomateria. 4 (2008) 535–543, https://doi.org/10.1016/j.actbio.2007.12.002.

[47] S. Nie, M. Tang, C. (Sage)Cheng, Z. Yin, L. Wang, S. Sun, C. Zhao, Biologically inspired membrane design with a heparin-like interface: prolonged blood coagulation, inhibited complement activation, and bio-artificial liver related cell proliferation, Biomater. Sci. 2 (2014) 98–109, https://doi.org/10.1039/C3BM60165J.
[48] J. Waser-Althaus, A. Salamon, M. Waser, C. Padeste, M. Kreutzer, U. Pieles, B. Müller, K. Peters, Differentiation of human mesenchymal stem cells on plasma-treated polyetheretherketone, J. Mater. Sci. - Mater. Med. 25 (2014) 515–525, https://doi.org/10.1007/s10856-013-5072-5.
[49] K. Anselme, M. Bigerelle, B. Noel, E. Dufresne, D. Judas, A. Iost, P. Hardouin, Qualitative and quantitative study of human osteoblast adhesion on materials with various surface roughnesses, J. Biomed. Mater. Res. 49 (2000) 155–166, https://doi.org/10.1002/(SICI)1097-4636(200002)49:2<155::AID-JBM2>3.0.CO;2-J.
[50] M. Verdanova, B. Rezek, A. Broz, E. Ukraintsev, O. Babchenko, A. Artemenko, T. Izak, A. Kromka, M. Kalbac, M. Hubalek Kalbacova, Nanocarbon allotropes-graphene and nanocrystalline diamond-promote cell proliferation, Small 12 (2016) 2499–2509, https://doi.org/10.1002/smll.201503749.
[51] L.-H. Han, S. Yu, T. Wang, A.W. Behn, F. Yang, Microribbon-like elastomers for fabricating macroporous and highly flexible scaffolds that support cell proliferation in 3D, Adv. Funct. Mater. 23 (2013) 346–358, https://doi.org/10.1002/adfm.201201212.
[52] X. Xie, A.M. Xu, M.R. Angle, N. Tayebi, P. Verma, N.A. Melosh, Mechanical model of vertical nanowire cell penetration, Nano Lett. 13 (2013) 6002–6008, https://doi.org/10.1021/nl403201a.
[53] J. Yan, W. Zhou, Z. Jia, P. Xiong, Y. Li, P. Wang, Q. Li, Y. Cheng, Y. Zheng, Endowing polyetheretherketone with synergistic bactericidal effects and improved osteogenic ability, Acta Biomateria. 79 (2018) 216–229, https://doi.org/10.1016/j.actbio.2018.08.037.
[54] L. Wang, S. He, X. Wu, S. Liang, Z. Mu, J. Wei, F. Deng, Y. Deng, S. Wei, Polyetheretherketone/nano-fluorohydroxyapatite composite with antimicrobial activity and osseointegration properties, Biomaterials 35 (2014) 6758–6775, https://doi.org/10.1016/j.biomaterials.2014.04.085.
[55] Y. Deng, L. Yang, X. Huang, J. Chen, X. Shi, W. Yang, M. Hong, Y. Wang, M.S. Dargusch, Z.-G. Chen, Dual Ag/ZnO-decorated micro-/nanoporous sulfonated polyetheretherketone with superior antibacterial capability and biocompatibility via layer-by-layer self-assembly strategy, Macromol. Biosci. 18 (2018) 1800028, https://doi.org/10.1002/mabi.201800028.

Supplementary materials

Dimension-dependent antibacterial behavior on bioactive micro/nano polyetheretherketone (PEEK) arrays

Shi Mo [1,2,a], Babak Mehrjou [1,a], Kaiwei Tang [1], Huaiyu Wang [2], Kaifu Huo [3], Abdul Mateen Qasim [1], Guomin Wang [1,*], Paul K Chu [1,*]

[1] *Department of Physics, Department of Materials Science and Engineering, and Department of Biomedical Engineering, City University of Hong Kong, Tat Chee Avenue, Kowloon, Hong Kong, China*

[2] *Shenzhen Institutes of Advanced Technology, Chinese Academy of Sciences, Shenzhen, China*

[3] *Wuhan National Laboratory for Optoelectronics (WNLO), School of Optical and Electronic Information, Huazhong University of Science and Technology, Wuhan, China*

[a] made equal contributions

* Corresponding authors: E-mail addresses: guomiwang2-c@my.cityu.edu.hk (G.M. Wang); paul.chu@cityu.edu.hk (P.K. Chu)

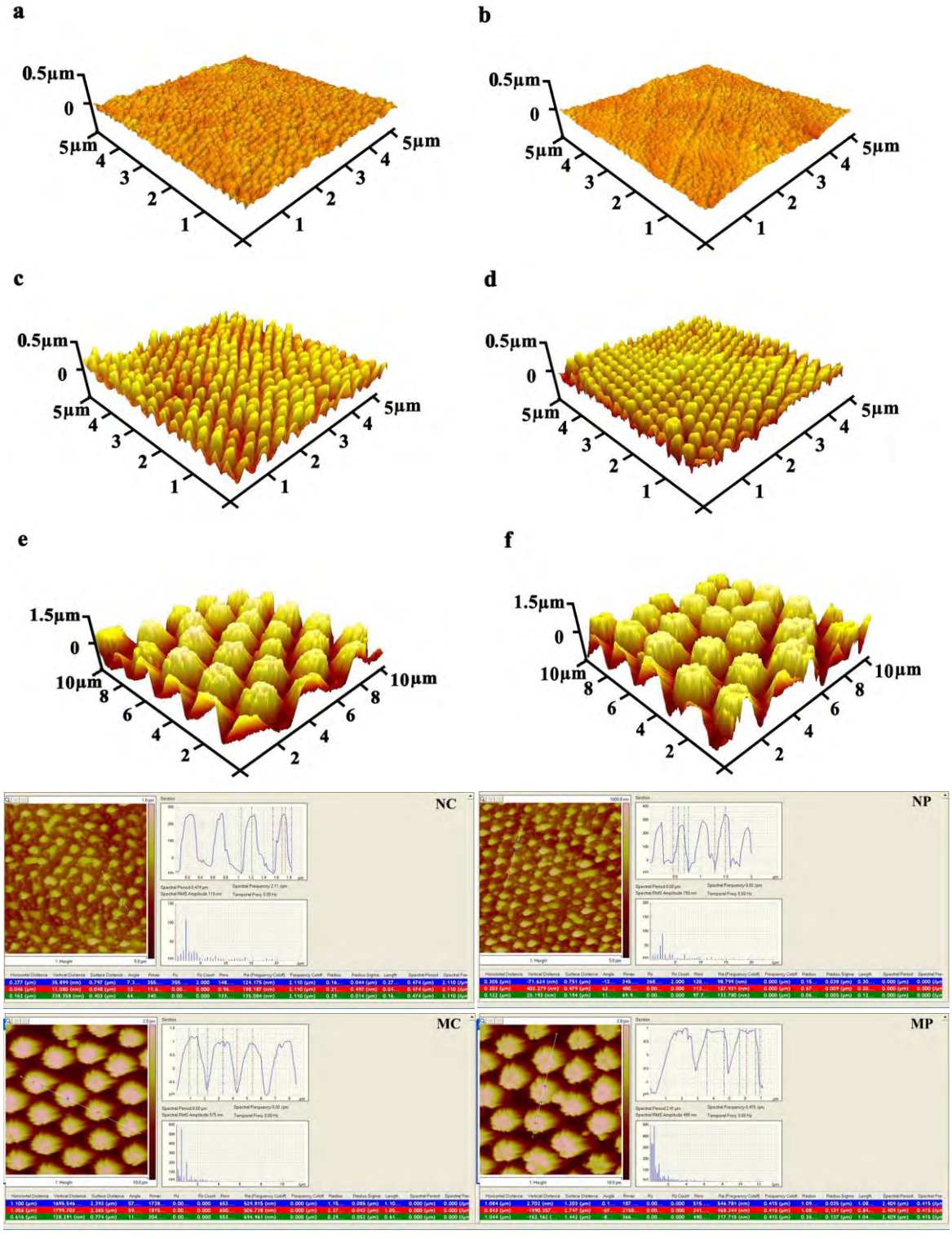

Figure S1. AFM images: (a) PEEK-Ar, (b) PEEK-O, (c) NC, (d) NP, (e) MC, and (f) MP. Bare samples treated with argon and oxygen plasma are denoted as PEEK-Ar and PEEK-O, respectively.

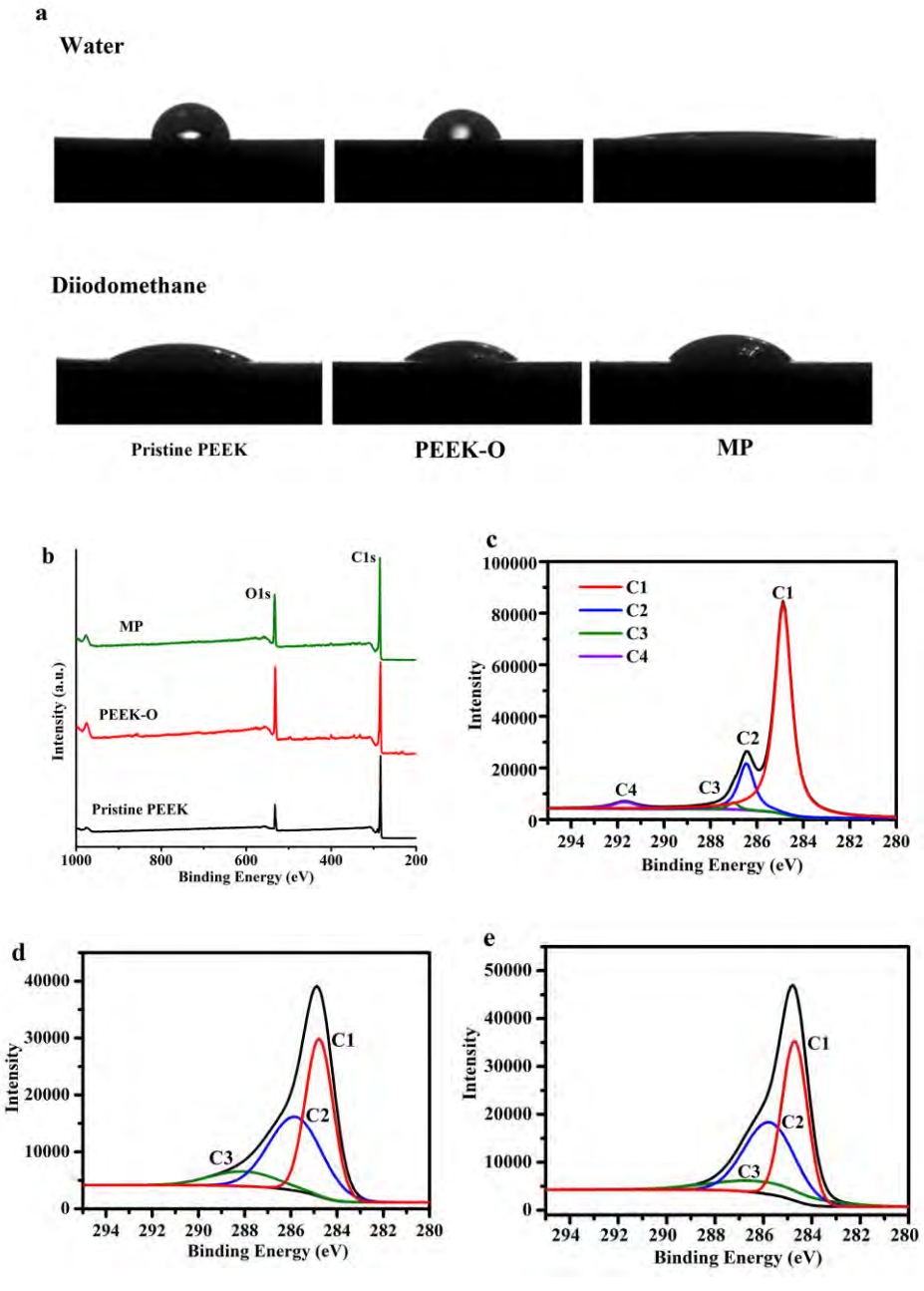

Figure S2 (a) Water and diiodomethane contact angles on pristine PEEK, PEEK-O, and MP; (b) XPS survey spectra; XPS C 1s spectra of (c) Pristine PEEK, (d) PEEK-O, and (e) MP.

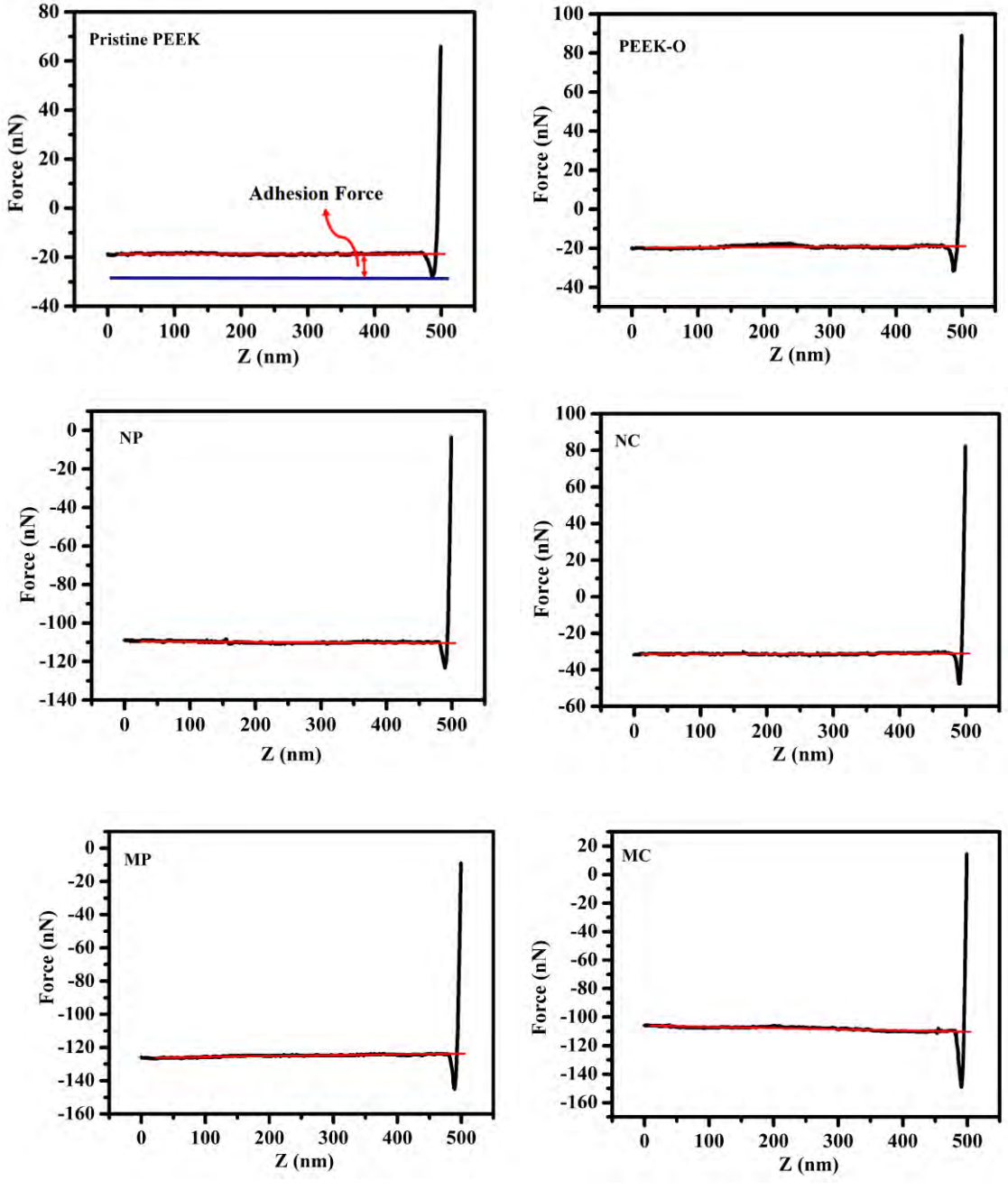

Figure S3 AFM measurement of the adhesion force between *E. coli* and sample surface.

Table S1. Plasma etching conditions.

Samples	Mask	Argon plasma (min)	Oxygen plasma (min)	Pressure (mTorr)	Power (W)
PEEK-Ar	No	15	/	21	50
PEEK-O	No	/	15	21	50
NC	0.32 μm	/	15	21	50
NP	0.32 μm	3	15	21	50
MC	1.5 μm	/	80	21	50
MP	1.5 μm	30	80	21	50

Table S2. Chemical compositions determined by XPS, contact angles, and surface energy of pristine PEEK, PEEK-O, and MP.

Samples	O (at%)	C (at%)	CA ^{O} (W)	CA ^{O} (O)	Surface Energy (mJ m^{-2})
Pristine PEEK	13.95	86.05	87.5	32.4	44.26
PEEK-O	27.79	72.21	77.1	40.6	49.59
MP	21.58	78.42	20.4	55.2	69.87